Commun. Comput. Phys.
doi: 10.4208/cicp.OA-2022-0085

Vol. **34**, No. 1, pp. 38-64
July 2023

Symmetry Preservation by a Compatible Staggered Lagrangian Scheme Using the Control-Volume Discretization Method in r–z Coordinate

Chunyuan Xu[1,*] and Qinghong Zeng[1]

[1] *Institute of Applied Physics and Computational Mathematics, Beijing 100091, China.*

Received 18 March 2022; Accepted (in revised version) 29 September 2022

Abstract. This paper aims at developing a control volume staggered Lagrangian scheme in r–z coordinate that preserves symmetry property. To achieve this goal, the support operator method is first utilized to derive the compatible discretization that satisfies the Geometrical Conservation Law (GCL) and momentum and total energy conservation property. We further introduce a method of source term treatment to recover the spherical symmetry of the current scheme. It is shown that the developed scheme has the benefit of maintaining the momentum and total energy conservation. The equi-angular grid, randomly distorted polar grid, and Cartesian grid are considered for one-dimensional spherical flow simulations. Also, an extension to the non-spherical flow is presented. The results confirm the good performance of the developed scheme.

AMS subject classifications: 65M08, 76M12

Key words: Symmetry preservation, compatibility, control-volume scheme, staggered Lagrangian scheme.

1 Introduction

Lagrangian methods [1–6] and the associated Arbitrary Lagrangian Eulerian (ALE) methods [7–11] nowadays constitute a standard approach to deal with high-speed compressible multimaterial flow problems. There are two main kinds of Lagrangian methods, namely the staggered and cell-centered Lagrangian methods. The staggered methods solve the governing equations in a non-conservative form. Numerous attempts have been conducted on them to make advances on the real-life applications [12–15]. The cell-centered methods, on the other hand, have gained much attention in recent years. They

*Corresponding author. *Email addresses:* xcyuan@mail.ustc.edu.cn (C. Xu), zeng_qinghong@iapcm.ac.cn (Q. Zeng)

are solved in a conservative form so that the solutions tend to a weak solution of the continuous problem.

The importance of symmetry property in Lagrangian methods is well recognized, especially when the flows are described in cylindrical geometry. For example, in a one-dimensional spherical flow, loss of symmetry will cause both the grid and variable fields to depart from a spherical shape as they evolve. Besides, in the case of extensions to non-symmetric flow problems, uncertainties can arise as to whether a nonsymmetric result comes from the physical process itself or from numerical error. Currently, cell-centered methods make better progress in symmetry preserving than staggered methods in that the conservative properties are preserved simultaneously [16–18]. However, any cell-centered method has a flaw that severe inaccuracy might occur in strong expansions, which is a potential obstacle for real-life applications [19].

Realizing the deficiency of cell-centered methods, it is important to promote the research of staggered methods as well. The focus of this work is symmetry preservation in a pure staggered Lagrangian framework. A simple way to achieve this goal is the employment of a "Cartesian form" of the momentum equation in cylindrical geometry. Methods developed in this way are usually called area-weighted methods [8, 20] because the integrations involved are performed in an area rather than a true volume. Area-weighted schemes are widely applied to real problem simulations, especially when discretization is done in a compatible manner. However, they can suffer from limitations due to their lack of momentum conservation. Another natural way to perform discretization is through the control-volume method. Caramana and Whalen [21] introduced a control-volume staggered method that preserves spherical symmetry and is not limited to an equi-angular polar grid. In their method, the gradient operator is modified in such a way that it fully recovers spherical symmetry and introduces only a very small change in the simulation results. Nevertheless, they found that this method, similar to the area-weighted method, does not strictly conserve momentum. In more recent work by Váchal and Wendroff [22], a so-called staggered GCS scheme was established using the control-volume method to preserve symmetry and total energy and reduce the GCL error to the order of the entropy error. Not enough is the investigation of total momentum conservation. Margolin and Shashkov [23] adopted a novel strategy to implement discretization on a curvilinear grid, and the scheme that they developed is able to preserve symmetry even on a nonuniform polar grid. Dobrev et al. [24] also developed a scheme on a curvilinear grid. Their method exactly conserves total energy and excels at preserving symmetry, while also avoiding the generation of spurious symmetry breaking near the rotation axis even for nonuniform grids.

Based on literature researches, the situation of symmetry preservation is less satisfactory in the non-curvilinear staggered methods, taking into account the conservative properties. To remedy the deficiency, the compatible discretization, whose weak consistency has been proved strictly [25], is first utilized in the current study. we use for reference to the methods [16–18] in which the symmetry and conservative properties are satisfied simultaneously by invoking a method of source term treatment. Consequently,

a control volume scheme that satisfies the GCL and momentum and total energy conservation is constructed. By taking full advantage of the total momentum conservation property, the staggered scheme further recovers the spherical symmetry in a concise way.

The remainder of this paper is organized as follows: In Section 2, we discuss total momentum conservation in cylindrical coordinates and review the basic Lagrangian equations. In Section 3, we implement a compatible spatial discretization. In Section 4, to recover the symmetry preservation property, we introduce a modification of the scheme developed in Section 3. In Section 5, we describe numerical simulations of some spherical flows to test the performance of the modified scheme. In Section 6, we present our concluding remarks and some perspectives.

2 Lagrangian hydrodynamics in two-dimensional cylindrical geometry

2.1 The issue of total momentum conservation

We are interested in Lagrangian hydrodynamics in a two-dimensional cylindrical geometry. Before discretizing the governing equations, this subsection first presents an important property of total momentum conservation, which has been mentioned in [8] and will be utilized to develop our new Lagrangian scheme.

An r–z coordinate system is established to describe an entity of revolution in the three-dimensional domain. As can be seen in Fig. 1, the angle between the r and x axes is θ. Thus, the unit coordinate vectors in the cylindrical system are

$$\boldsymbol{e}_r=(\cos\theta,\sin\theta,0),\quad \boldsymbol{e}_z=(0,0,1),\quad \boldsymbol{e}_\theta=(-\sin\theta,\cos\theta,0). \tag{2.1}$$

Let $\boldsymbol{U}(r,z,\theta,t)$ denote the velocity vector in an axisymmetric problem. The θ component of velocity is zero, and the other components do not depend on θ, so that

$$\boldsymbol{U}(r,z,\theta,t)=u(r,z,t)\boldsymbol{e}_r(\theta)+v(r,z,t)\boldsymbol{e}_z, \tag{2.2}$$

where u and v are the velocity components along the r and z axes. The total momentum at time t is defined as follows:

$$\boldsymbol{M}(t)=\int_{V(t)}\rho\boldsymbol{U}dV, \tag{2.3}$$

where ρ is the density and does not depend on θ. Substitution of Eq. (2.2) into Eq. (2.3) gives

$$\begin{aligned}\boldsymbol{M}(t)=&\int_{A(t)}u(r,z,t)\rho(r,z,t)rdrdz\int_0^{2\pi}\boldsymbol{e}_r(\theta)d\theta\\&+2\pi\boldsymbol{e}_z\int_{A(t)}v(r,z,t)\rho(r,z,t)rdrdz,\end{aligned} \tag{2.4}$$

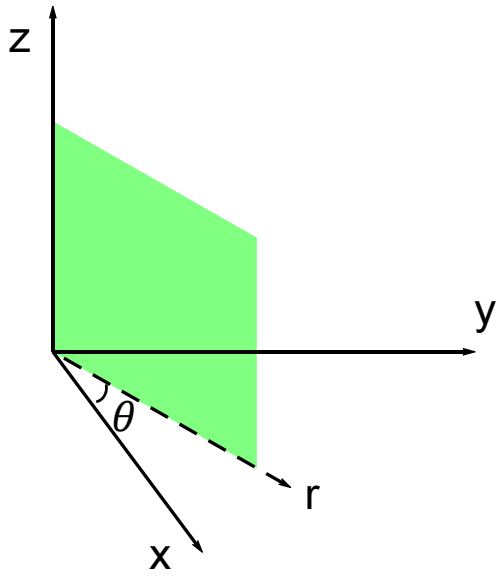

Figure 1: Cylindrical coordinates in three-dimensional domain.

which can be further simplified since $\int_0^{2\pi} \boldsymbol{e}_r(\theta)d\theta = 0$:

$$\boldsymbol{M}(t) = 2\pi \boldsymbol{e}_z \int_{A(t)} v(r,z,t)\rho(r,z,t) r dr dz. \tag{2.5}$$

It can be deduced from Eq. (2.5) that total momentum conservation ($d\boldsymbol{M}(t)/dt = 0$) does not depend on the r component of the velocity, and only involves the z component. This property will be used in the discretization procedure to develop a symmetry-preserving scheme.

2.2 Basic equations

The basic equations of staggered Lagrangian hydrodynamics comprise the Lagrangian representation of a moving fluid element, the momentum equation, and the equation for evolution of the specific internal energy. These can be written as follows:

$$\rho \frac{d}{dt}\left(\frac{1}{\rho}\right) - \nabla \cdot \boldsymbol{U} = 0, \tag{2.6a}$$

$$\rho \frac{d\boldsymbol{U}}{dt} + \nabla P = 0, \tag{2.6b}$$

$$\rho \frac{d\varepsilon}{dt} + P \nabla \cdot \boldsymbol{U} = 0, \tag{2.6c}$$

where ρ is the density, $\boldsymbol{U}$ is the velocity, P is the pressure, and ε is the specific internal energy. The operator $\nabla\cdot\boldsymbol{U}$ determines the volume evolution of an arbitrary fluid element, and it can be implemented in two different ways. First, by application of Gauss's theorem and specification of a set of velocities the discrete form of $\nabla\cdot\boldsymbol{U}$ can be obtained. Second, given the point coordinates that constitute the fluid element, the volume V can be computed, and differentiation of V with respect to time also provides the discrete form of $\nabla\cdot\boldsymbol{U}$. It is known that this second method is linked to the trajectory equation,

$$\frac{d\boldsymbol{X}}{dt}=\boldsymbol{U}(\boldsymbol{X}(t),t),\quad \boldsymbol{X}(0)=\boldsymbol{X}_0. \tag{2.7}$$

Any Lagrangian scheme that utilizes these two methods of discretization in an equivalent manner is said to satisfy the GCL.

Finally, the equation of state of an ideal gas is adopted to close the basic equations:

$$P=(\gamma-1)\rho\varepsilon. \tag{2.8}$$

2.3 Derivation of momentum equation

The integral form of the momentum equation over the volume V is derived in [4], and would be introduced here briefly.

In a cylindrical coordinate system, the divergence operator has the form

$$\nabla\cdot\boldsymbol{U}=\frac{\partial u}{\partial z}+\frac{1}{r}\frac{\partial(rv)}{\partial r}=\frac{\partial u}{\partial z}+\frac{\partial v}{\partial r}+\frac{v}{r}, \tag{2.9}$$

if $\boldsymbol{U}$ is constant, then the following relation is satisfied:

$$\nabla\cdot\boldsymbol{U}=\frac{1}{r}\boldsymbol{U}\cdot\boldsymbol{e}_r. \tag{2.10}$$

After integrating the momentum equation Eq. (2.6b) over the volume V, it has,

$$\frac{d}{dt}\int_V\rho\boldsymbol{U}dV+\int_V\nabla PdV=0. \tag{2.11}$$

Utilizing Eq. (2.10) and the relation $\nabla\cdot(P\boldsymbol{U})=\boldsymbol{U}\cdot\nabla P+P\nabla\cdot\boldsymbol{U}$, it gives

$$\int_V\nabla PdV=\int_L P\boldsymbol{N}rdL-\boldsymbol{e}_r\int_A PdA, \tag{2.12}$$

Substitution of Eq. (2.12) into Eq. (2.11) gives

$$\frac{d}{dt}\int_V\rho\boldsymbol{U}dV+\int_L P\boldsymbol{N}rdL-\boldsymbol{e}_r\int_A PdA=0, \tag{2.13}$$

where L is the boundary of the Lagrangian volume on the r–z plane, and A is the area of the closed region surrounded by L.

3 Spatial discretization

This section considers the spatial discretization of a staggered Lagrangian scheme. The discretization is implemented together with the support operator method [1] in a compatible manner so that the total energy is conserved.

3.1 Notation

Fig. 2 shows the geometric objects in staggered Lagrangian hydrodynamics, namely, the cell object Ω_c and the point object Ω_p. Basically, Ω_p is constructed by connecting the centroid of cells around point p and the midpoints of the edges associated with it in sequence. The discrete geometric element Ω_p is called the dual grid in the following for simplicity. A Lagrangian object, the subcell mass m_{cp}, is introduced such that

$$m_c = \sum_{p\in\mathcal{P}(c)} m_{cp}, \quad m_p = \sum_{c\in\mathcal{C}(p)} m_{cp}, \tag{3.1}$$

where m_{cp} is invariant with respect to time t, m_p is the mass of Ω_p, and m_c is the mass of Ω_c. $\mathcal{P}(c)$ is the set of points around cell c, and $\mathcal{C}(p)$ is the set of cells around point p.

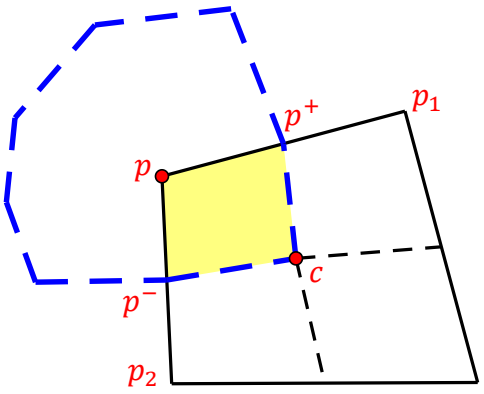

Figure 2: Geometric objects in staggered Lagrangian hydrodynamics.

3.2 Discrete support operators

After integration of Eq. (2.6a) over an arbitrary cell Ω_c and application of the finite volume method, its discrete form is obtained as follows:

$$\frac{dV_c}{dt} = \sum_{\mathcal{F}(c)} r_{pp'} L_{pp'} \boldsymbol{N}_{pp'} \cdot \boldsymbol{u}_{pp'}, \tag{3.2}$$

where $\mathcal{F}(c)$ is the set of faces (edges) of the cell, and the subscript pp' denotes the two endpoints of a generic face of cell c. $L_{pp'}$ and $\boldsymbol{N}_{pp'}$ are the length and unit outward vector

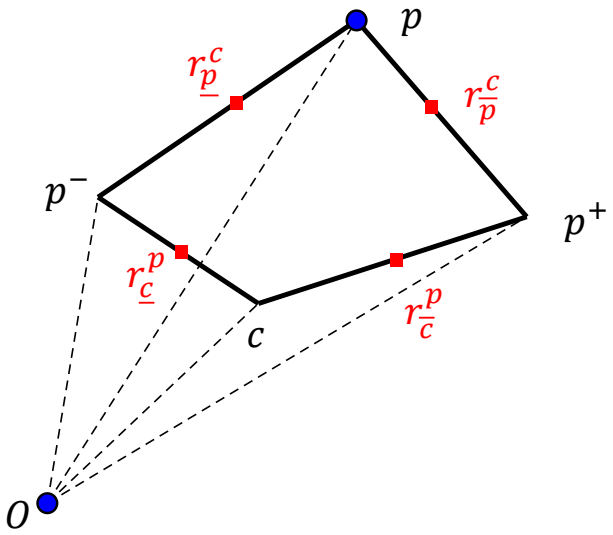

Figure 3: Triangular decomposition of the subcell Ω_c^p.

of the face. $r_{pp'}$ is the weighted value of the r coordinate r_p and $r_{p'}$, and $\boldsymbol{U}_{pp'}$ is the weighted value of point velocity $\boldsymbol{U}_p$ and $\boldsymbol{U}_{p'}$. Furthermore, if the midpoints of the edges adjacent to point p in cell c are p^+ and p^-, then the half-face discretization of the volume equation can be written as

$$\frac{dV_c}{dt}-\sum_{p\in\mathcal{P}(c)}\left(r_{\overline{p}}^c L_{\overline{p}}^c \boldsymbol{U}_{\overline{p}}^c\cdot\boldsymbol{N}_{\overline{p}}^c+r_{\underline{p}}^c L_{\underline{p}}^c \boldsymbol{U}_{\underline{p}}^c\cdot\boldsymbol{N}_{\underline{p}}^c\right)=0, \tag{3.3}$$

where subscripts $\overline{p}$ and $\underline{p}$ are associated with the half-edges pp^+ and pp^-, respectively. Similar to $r_{pp'}$ and $\boldsymbol{U}_{pp'}$, $r_{\overline{p}}^c$,$r_{\underline{p}}^c$,$\boldsymbol{U}_{\overline{p}}^c$ and $\boldsymbol{U}_{\underline{p}}^c$ are weighted values. $L_{\overline{p}}^c$ and $L_{\underline{p}}^c$ are half-edge lengths, and $\boldsymbol{N}_{\overline{p}}^c$ and $\boldsymbol{N}_{\underline{p}}^c$ are unit outward vectors of the half-edges.

The volume of cell Ω_c can be computed by performing the triangular decomposition. An example is given in Fig. 3 to show how the decomposition is implemented in a subcell. By using Pappus's rule [26], the volume per radian of the cell is computed as

$$\begin{aligned}V_c=\frac{1}{2}\sum_{p\in\mathcal{P}'(c)}\frac{1}{3}\big[&\left(r_O+r_p+r_{p^+}\right)\left(\boldsymbol{X}_p\times\boldsymbol{X}_{p^+}\right)\\&+\left(r_O+r_p+r_{p^-}\right)\left(\boldsymbol{X}_p\times\boldsymbol{X}_{p^-}\right)\big]\cdot\boldsymbol{e}_Z,\end{aligned} \tag{3.4}$$

where $\mathcal{P}'(c)$ is the set of cell points and edge midpoints around a point, and $\boldsymbol{e}_Z=\boldsymbol{e}_X\times\boldsymbol{e}_Y$. The time derivative of this equation is

$$\frac{dV_c}{dt}=\frac{1}{2}\sum_{p\in\mathcal{P}'(c)}\left(\frac{2r_p+r_{p^+}}{3}L_{\overline{p}}^c\boldsymbol{N}_{\overline{p}}^c+\frac{2r_p+r_{p^-}}{3}L_{\underline{p}}^c\boldsymbol{N}_{\underline{p}}^c\right)\cdot\boldsymbol{U}_p. \tag{3.5}$$

By requiring the equivalence of Eqs. (3.3) and (3.5), the GCL is satisfied:

$$r^c_{\overline{p}}\boldsymbol{U}^c_{\overline{p}}=\frac{1}{2}\left(\frac{2r_p+r_{p^+}}{3}\boldsymbol{U}_p+\frac{r_p+2r_{p^+}}{3}\boldsymbol{U}_{p^+}\right), \tag{3.6a}$$

$$r^c_{\underline{p}}\boldsymbol{U}^c_{\underline{p}}=\frac{1}{2}\left(\frac{2r_p+r_{p^-}}{3}\boldsymbol{U}_p+\frac{r_p+2r_{p^-}}{3}\boldsymbol{U}_{p^-}\right). \tag{3.6b}$$

As shown in Fig. 3, if the velocity along the half-edges pp^+ and pp^- is assumed to be a constant equal to $\boldsymbol{U}_p$, then

$$\begin{aligned} &r^c_{\overline{p}}=\frac{1}{2}\left(r_p+r_{p^+}\right), && r^c_{\underline{p}}=\frac{1}{2}\left(r_p+r_{p^-}\right),\\ &\boldsymbol{N}^c_{\overline{p}}=\boldsymbol{N}_{pp^+}, && \boldsymbol{N}^c_{\underline{p}}=\boldsymbol{N}_{pp^-},\\ &L^c_{\overline{p}}=L_{pp^+}, && L^c_{\underline{p}}=L_{pp^-}. \end{aligned} \tag{3.7}$$

The discrete form of the divergence operator that satisfies the GCL is thus represented as

$$(\nabla\cdot\boldsymbol{U})_{p\to c}=\frac{1}{V_c}\frac{dV_c}{dt}=\frac{1}{V_c}\sum_{p\in\mathcal{P}(c)}\left(r^c_{\overline{p}}L^c_{\overline{p}}\boldsymbol{N}^c_{\overline{p}}+r^c_{\underline{p}}L^c_{\underline{p}}\boldsymbol{N}^c_{\underline{p}}\right)\cdot\boldsymbol{U}_p, \tag{3.8}$$

where the subscript $p\to c$ indicates that the operator acts from points to cells. Similarly, the divergence operator acting from cells to points is defined as

$$(\nabla\cdot\boldsymbol{U})_{c\to p}=\frac{1}{V_p}\frac{dV_p}{dt}=\frac{1}{V_p}\sum_{c\in\mathcal{C}(p)}\left(r^p_{\overline{c}}L^p_{\overline{c}}\boldsymbol{N}^p_{\overline{c}}+r^p_{\underline{c}}L^p_{\underline{c}}\boldsymbol{N}^p_{\underline{c}}\right)\cdot\boldsymbol{U}_c, \tag{3.9}$$

where $\mathcal{C}(p)$ is the set of cell centers around point p. The velocity along the half-edges cp^+ and cp^- is assumed to be a constant equal to $\boldsymbol{U}_c$, and the following notation is adopted:

$$\begin{aligned} &r^p_{\overline{c}}=\frac{1}{2}\left(r_c+r_{p^+}\right), && r^p_{\underline{c}}=\frac{1}{2}\left(r_c+r_{p^-}\right),\\ &\boldsymbol{N}^p_{\overline{c}}=\boldsymbol{N}_{cp^+}, && \boldsymbol{N}^p_{\underline{c}}=\boldsymbol{N}_{cp^-},\\ &L^p_{\overline{c}}=L_{cp^+}, && L^p_{\underline{c}}=L_{cp^-}. \end{aligned} \tag{3.10}$$

We will now show how the basic equations are discretized in a compatible way based on the divergence operators. Basically, the discretization described below is an extension of work [27] from the Cartesian coordinate to cylindrical coordinate.

3.3 Compatible discretization

Integration of the momentum equation (2.13) over the dual grids gives

$$m_p\frac{d\boldsymbol{U}_p}{dt}+\int_{L_p}P\boldsymbol{N}rdL-\boldsymbol{e}_r\int_{A_p}PdA=0. \tag{3.11}$$

Under the assumption that two pressures $\Pi_{\underline{c}}^p$ and $\Pi_{\overline{c}}^p$ are associated with the half-edges cp^+ and cp^-, the discrete gradient operator $(\nabla P)_{c\to p}$ is defined in a manner that is consistent with the definition of the divergence operator $(\nabla\cdot\boldsymbol{U})_{c\to p}$:

$$(\nabla P)_{c\to p}=\frac{1}{V_p}\sum_{c\in\mathcal{C}(p)}\left(r_{\underline{c}}^p L_{\underline{c}}^p\Pi_{\underline{c}}^p\boldsymbol{N}_{\underline{c}}^p+r_{\overline{c}}^p L_{\overline{c}}^p\Pi_{\overline{c}}^p\boldsymbol{N}_{\overline{c}}^p-P_c A_c^p\boldsymbol{e}_r\right), \tag{3.12}$$

where P_c is the pressure of cell Ω_c, and A_c^p is the area of subcell Ω_c^p. To simplify the notation in this definition, the flux and source terms are denoted by $\boldsymbol{F}_{cp}$ and $\boldsymbol{S}_{cp}$, respectively:

$$\boldsymbol{F}_{cp}=r_{\underline{c}}^p L_{\underline{c}}^p\Pi_{\underline{c}}^p\boldsymbol{N}_{\underline{c}}^p+r_{\overline{c}}^p L_{\overline{c}}^p\Pi_{\overline{c}}^p\boldsymbol{N}_{\overline{c}}^p,\quad \boldsymbol{S}_{cp}=P_c A_c^p\boldsymbol{e}_r. \tag{3.13}$$

Using this notation, the semidiscrete momentum equation is written as

$$m_p\frac{d\boldsymbol{U}_p}{dt}+\sum_{c\in\mathcal{C}(p)}\left(\boldsymbol{F}_{cp}-\boldsymbol{S}_{cp}\right)=0. \tag{3.14}$$

The total energy is defined as the sum of the total kinetic energy and total internal energy: $E=\mathcal{K}+\mathcal{E}$. Total energy conservation without consideration of boundary conditions is then described as follows:

$$\frac{dE}{dt}=\frac{d\mathcal{K}}{dt}+\frac{d\mathcal{E}}{dt}=\frac{1}{2}\sum_p m_p\frac{d(\boldsymbol{U}_p\cdot\boldsymbol{U}_p)}{dt}+\sum_c m_c\frac{d\varepsilon_c}{dt}=0. \tag{3.15}$$

Use of the semidiscrete momentum equation yields

$$\sum_c m_c\frac{d\varepsilon_c}{dt}-\sum_p\sum_{c\in\mathcal{C}(p)}\left(\boldsymbol{F}_{cp}-\boldsymbol{S}_{cp}\right)\cdot\boldsymbol{U}_p=0, \tag{3.16}$$

and interchanging the order of the double summation yields

$$\sum_c\left[m_c\frac{d\varepsilon_c}{dt}-\sum_{p\in\mathcal{P}(c)}\left(\boldsymbol{F}_{cp}-\boldsymbol{S}_{cp}\right)\cdot\boldsymbol{U}_p\right]=0. \tag{3.17}$$

Thus, a sufficient condition for conservation of total energy is that this equation holds in an arbitrary cell, i.e.,

$$m_c\frac{d\varepsilon_c}{dt}-\sum_{p\in\mathcal{P}(c)}\left(\boldsymbol{F}_{cp}-\boldsymbol{S}_{cp}\right)\cdot\boldsymbol{U}_p=0. \tag{3.18}$$

By using an entropy conservation approximation, Eq. (3.18) can be written as

$$m_c\frac{d\varepsilon_c}{dt}-P_c\sum_{p\in\mathcal{P}(c)}\left(\boldsymbol{G}_c-A_c^p\boldsymbol{e}_r\right)\cdot\boldsymbol{U}_p=0, \tag{3.19}$$

where the geometric vector $\boldsymbol{G}_c = r^p_{\underline{c}} L^p_{\underline{c}} \boldsymbol{N}^p_{\underline{c}} + r^p_{\overline{c}} L^p_{\overline{c}} \boldsymbol{N}^p_{\overline{c}}$. From Eq. (2.12), it can be seen that for constant pressure, the following relation holds:

$$\int_L \boldsymbol{N} r dL = A \boldsymbol{e}_r. \tag{3.20}$$

Substituting Eq. (3.20) into Eq. (3.19) yields

$$m_c \frac{d\varepsilon_c}{dt} + P_c \sum_{p \in \mathcal{P}(c)} \boldsymbol{G}_p \cdot \boldsymbol{U}_p = 0, \tag{3.21}$$

where the geometric vector $\boldsymbol{G}_p = r^c_{\overline{p}} L^c_{\overline{p}} \boldsymbol{N}^c_{\overline{p}} + r^c_{\underline{p}} L^c_{\underline{p}} \boldsymbol{N}^c_{\underline{p}}$, and $\boldsymbol{G}_c + \boldsymbol{G}_p = A^p_c \boldsymbol{e}_r$. Together, Eqs. (3.8) and (3.21) yield

$$m_c \frac{d\varepsilon_c}{dt} + P_c V_c (\nabla \cdot \boldsymbol{U})_{p \to c} = 0. \tag{3.22}$$

It is known that $(\nabla \cdot \boldsymbol{U})_{p \to c}$ can be deduced from the GCL condition, which implies that the volume associated with the internal energy is equivalent to that associated with the point coordinates. Therefore, the compatible discretization satisfies the GCL.

Finally, the semidiscrete finite volume scheme with the primary variables $(\boldsymbol{U}_p, \varepsilon_c, \boldsymbol{X}_p)$ is obtained as follows:

$$\begin{aligned} &m_p \frac{d\boldsymbol{U}_p}{dt} + \sum_{c \in \mathcal{C}(p)} (\boldsymbol{F}_{cp} - \boldsymbol{S}_{cp}) = 0, \\ &m_c \frac{d\varepsilon_c}{dt} - \sum_{p \in \mathcal{P}(c)} (\boldsymbol{F}_{cp} - \boldsymbol{S}_{cp}) \cdot \boldsymbol{U}_p = 0, \\ &\frac{d\boldsymbol{X}}{dt} = \boldsymbol{U}(\boldsymbol{X}(t), t), \quad \boldsymbol{X}(0) = \boldsymbol{X}_0. \end{aligned} \tag{3.23}$$

Note that the cell density is updated by dividing the cell mass by the volume computed from the trajectory equation.

3.4 Shock capturing

A cell-centered Riemann solver [27] is applied to deal with shock capturing mechanisms. The pressures in Eq. (3.12) are obtained using the following half-Riemann problems:

$$\begin{aligned} P_c - \Pi^p_{\underline{c}} &= Z^p_{\underline{c}} \Delta \boldsymbol{U}_{cp} \cdot \boldsymbol{N}^p_{\underline{c}}, \\ P_c - \Pi^p_{\overline{c}} &= Z^p_{\overline{c}} \Delta \boldsymbol{U}_{cp} \cdot \boldsymbol{N}^p_{\overline{c}}, \end{aligned} \tag{3.24}$$

where $\Delta \boldsymbol{U}_{cp} = \boldsymbol{U}_c - \boldsymbol{U}_p$ is the difference between the cell-center and point velocities. $Z^p_{\underline{c}}$ and $Z^p_{\overline{c}}$ are the swept mass fluxes, defined as

$$Z^p_{\underline{c}} = Z^p_{\overline{c}} = \rho_c (a_c + \Gamma_c |\Delta \boldsymbol{U}_{cp} \cdot \boldsymbol{N}_{cp}|), \tag{3.25}$$

where $\boldsymbol{N}_{cp}$ is a unit vector perpendicular to the line cp, a_c is the speed of sound, and Γ_c is a material-dependent coefficient given by

$$\Gamma_c = \begin{cases} \dfrac{\gamma+1}{2} & \text{if } (\nabla\cdot\boldsymbol{U})_{cp} < 0, \\ 0 & \text{if } (\nabla\cdot\boldsymbol{U})_{cp} \geq 0, \end{cases} \tag{3.26}$$

where $(\nabla\cdot\boldsymbol{U})_{cp}$ is defined as

$$(\nabla\cdot\boldsymbol{U})_{cp} = -\frac{1}{V_{cp}}\left(L_{\bar{c}}^{p}\boldsymbol{N}_{\bar{c}}^{p} + L_{\underline{c}}^{p}\boldsymbol{N}_{\underline{c}}^{p}\right)\cdot\Delta\boldsymbol{U}_{cp}. \tag{3.27}$$

Substitution of Eq. (3.24) into Eq. (3.13) yields

$$\boldsymbol{F}_{cp} = \left(r_{\underline{c}}^{p}L_{\underline{c}}^{p}\boldsymbol{N}_{\underline{c}}^{p} + r_{\bar{c}}^{p}L_{\bar{c}}^{p}\boldsymbol{N}_{\bar{c}}^{p}\right)P_c - M_{cp}\Delta\boldsymbol{U}_{cp}, \tag{3.28}$$

where M_{cp} is a 2×2 positive-definite matrix,

$$M_{cp} = Z_{\underline{c}}^{p}r_{\underline{c}}^{p}L_{\underline{c}}^{p}\boldsymbol{N}_{\underline{c}}^{p}\otimes\boldsymbol{N}_{\underline{c}}^{p} + Z_{\bar{c}}^{p}r_{\bar{c}}^{p}L_{\bar{c}}^{p}\boldsymbol{N}_{\bar{c}}^{p}\otimes\boldsymbol{N}_{\bar{c}}^{p}. \tag{3.29}$$

Summation of the momentum equation over the dual grids leads to

$$\frac{d}{dt}\left(\sum_p m_p\boldsymbol{U}_p\right) = -\sum_p\sum_{c\in\mathcal{C}(p)}\left(\boldsymbol{F}_{cp} - \boldsymbol{S}_{cp}\right), \tag{3.30}$$

the source term $\boldsymbol{S}_{cp}$ has only a radial component, and it does not influence total momentum conservation. Therefore, the above equation is simplified as

$$\frac{d}{dt}\left(\sum_p m_p\boldsymbol{U}_p\right) = -\sum_p\sum_{c\in\mathcal{C}(p)}\boldsymbol{F}_{cp}, \tag{3.31}$$

interchanging the order of the double summation yields

$$\frac{d}{dt}\left(\sum_p m_p\boldsymbol{U}_p\right) = -\sum_c\sum_{p\in\mathcal{P}(c)}\boldsymbol{F}_{cp}. \tag{3.32}$$

A sufficient condition to satisfy the total momentum conservation is

$$\sum_{p\in\mathcal{P}(c)}\boldsymbol{F}_{cp} = 0. \tag{3.33}$$

Together, Eqs. (3.28) and (3.33) provide a method to compute the cell center velocity $\boldsymbol{U}_c$ iteratively:

$$\boldsymbol{U}_c = M_c^{-1}\sum_{p\in\mathcal{P}(c)}M_{cp}\boldsymbol{U}_p, \tag{3.34}$$

where $M_c = \sum_{p\in\mathcal{P}(c)}M_{cp}$. Since M_c is a positive-definite matrix, it is always invertible. The presence of the swept mass fluxes in M_{cp} makes Eq. (3.34) a nonlinear system. In practice, only a few iterations are needed to reach convergence. Once $\boldsymbol{U}_c$ has been computed, Eqs. (3.23) are updated explicitly and in sequence to advance the current time step.

3.5 Entropy inequality

Use of the Gibbs relation for the cell Ω_c gives

$$m_c T_c \frac{dS_c}{dt} = m_c \left[\frac{d\varepsilon_c}{dt} + P_c \frac{d}{dt}\left(\frac{1}{\rho_c}\right)\right]. \tag{3.35}$$

Substitution of Eqs. (3.8) and (3.18) into Eq. (3.35) gives

$$m_c T_c \frac{dS_c}{dt} = \sum_{p\in\mathcal{P}(c)} \left(\boldsymbol{F}_{cp} - \boldsymbol{S}_{cp} + P_c \boldsymbol{G}_p\right)\cdot \boldsymbol{U}_p. \tag{3.36}$$

This equation still holds in another frame with constant velocity $\boldsymbol{U}_c$:

$$m_c T_c \frac{dS_c}{dt} = \sum_{p\in\mathcal{P}(c)} \left(\boldsymbol{F}_{cp} - \boldsymbol{S}_{cp} + P_c \boldsymbol{G}_p\right)\cdot \left(\boldsymbol{U}_p - \boldsymbol{U}_c\right). \tag{3.37}$$

Together, Eqs. (3.20), (3.28), and (3.37) give

$$\begin{aligned} m_c T_c \frac{dS_c}{dt} &= \sum_{p\in\mathcal{P}(c)} \left[P_c \boldsymbol{G}_p - M_{cp}\Delta \boldsymbol{U}_{cp} - P_c\left(\boldsymbol{G}_c + \boldsymbol{G}_p\right) + P_c \boldsymbol{G}_c\right]\cdot\left(\boldsymbol{U}_p - \boldsymbol{U}_c\right) \\ &= \sum_{p\in\mathcal{P}(c)} M_{cp}(\boldsymbol{U}_p - \boldsymbol{U}_c)^2. \end{aligned} \tag{3.38}$$

Since M_{cp} is a positive-definite matrix, the entropy inequality is always satisfied.

4 Recovering spherical symmetry of the scheme

The control-volume scheme in Eq. (3.23) has many good properties, such as the GCL, entropy inequality, and momentum and total energy conservation. However, it has the limitation that it does not preserve symmetry for spherical flows. In this section, utilizing the total momentum conservation property in Eq. (2.5), we recover the spherical symmetry property of this scheme by a proper treatment of the source term. The treatment is conducted simultaneously in the momentum and internal energy equations so that the total energy is conserved.

As can be seen in Fig. 4, an equi-angular polar grid is generated on the cylindrical coordinate system. The radial and angular divisions are K and L. Point and cell-center indices are represented by integers (i,j) and half-integers $(i-\frac{1}{2},j-\frac{1}{2})$. Connecting an arbitrary point (i,j) to the origin, the angle between the connected line and the z axis is φ. The dual grid Ω_p consists of four cell centers labeled 1, 2, 3, and 4, and four edge midpoints labeled a, b, c, and d. The grid points in the neighborhood of p are p_1, p_2, p_3, and p_4. A perpendicular line is drawn from edge midpoints b and d to the radial edge pp_1, and the intersection is f. Another perpendicular line is drawn from cell centers 1 and

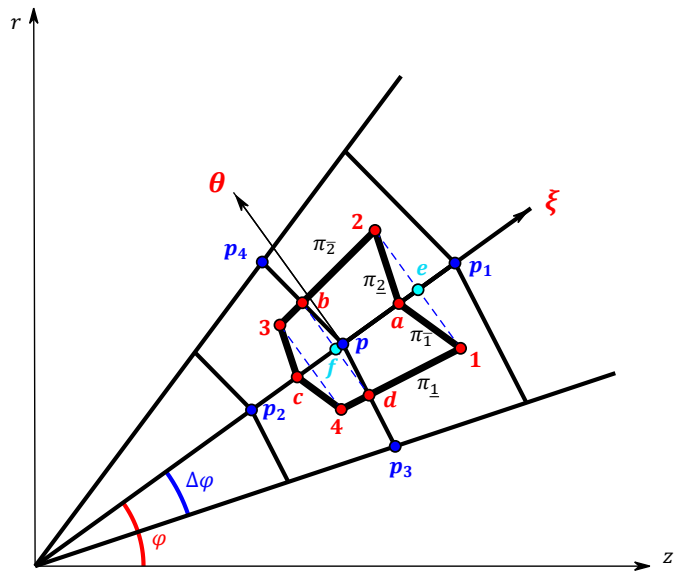

Figure 4: Equi-angular polar grid for the treatment of the source term.

2 to the radial edge pp_1, and the intersection is e. In the subcells Ω_1^p and Ω_2^p, the symbols in Eq. (3.12) are used to denote geometric and physical variables, and the superscripts are omitted for simplicity. In the triangles $1ae$, $2ae$, dpf, and bpf, the lengths of the edges $1e$, $2e$, df, and bf are denoted by $L'_{\bar{1}}$, $L'_{\underline{2}}$, $L''_{\bar{1}}$, and $L''_{\underline{2}}$, respectively. The unit outward normals are denoted by $\boldsymbol{N}'_{\bar{1}}$, $\boldsymbol{N}'_{\underline{2}}$, $\boldsymbol{N}''_{\bar{1}}$, and $\boldsymbol{N}''_{\underline{2}}$, respectively. A local coordinate system (ξ,θ) is constructed around p, with the ξ and θ axes respectively parallel and perpendicular to the edge pp_1. The distances from points e, p, and f to the origin are denoted by d_e, d_p, and d_f, respectively. For a given polygon, its area is denoted by A with subscripts consisting of its grid points.

We will now describe how the source term is treated to recover spherical symmetry, taking as an example the subcell Ω_1^p.

4.1 Treatment of source term

According to Eq. (2.5), modification of radial component of the momentum does not affect total momentum conservation. This property provides an alternative way to construct symmetry preserving Lagrangian schemes, namely, a treatment of the source term along the radial direction. Utilizing this idea, some cell-centered Lagrangian schemes [16–18] using quadrilateral mesh have been developed.

In the current staggered Lagrangian scheme, the dual grid is octagonal to make the geometric feature more complicated. A treatment of source term is thus developed adap-

tively. To be specific, the source term $\boldsymbol{S}_{cp}$ in Eq. (3.23) for the subcell Ω_1^p is written as

$$\boldsymbol{S}_{1p} = P_1 A_{1apd} \boldsymbol{e}_r. \tag{4.1}$$

Eq. (4.1) is then replaced by the following expression in the numerical scheme to recover spherical symmetry:

$$\boldsymbol{S}_{1p}^* = \begin{cases} \left(\Pi_{\underline{1}} A_{1efd} - \Pi_{\bar{1}} A_{ae1}\right) \mathbf{e}_r & \text{if } \overrightarrow{ap} \cdot \overrightarrow{ae} < 0, \\ \left(\Pi_{\underline{1}} A_{1efd} + \Pi_{\bar{1}} A_{ae1}\right) \mathbf{e}_r & \text{if } \overrightarrow{ap} \cdot \overrightarrow{ae} \geq 0. \end{cases} \tag{4.2}$$

It should be emphasized that this operation can be easily extended to other subcells of the dual grid, but the details are omitted here to save space.

With the modified source term, the scheme (3.23) is rewritten as

$$\begin{aligned} & m_p \frac{d\boldsymbol{U}_p}{dt} + \sum_{c \in \mathcal{C}(p)} \left(\boldsymbol{F}_{cp} - \boldsymbol{S}_{cp}^* \right) = 0, \\ & m_c \frac{d\varepsilon_c}{dt} - \sum_{p \in \mathcal{P}(c)} \left(\boldsymbol{F}_{cp} - \boldsymbol{S}_{cp}^* \right) \cdot \boldsymbol{U}_p = 0, \\ & \frac{d\boldsymbol{X}}{dt} = \boldsymbol{U}(\boldsymbol{X}(t), t), \quad \boldsymbol{X}(0) = \boldsymbol{X}_0. \end{aligned} \tag{4.3}$$

Compared with the scheme (3.23), the modified scheme (4.3) still ensures conservation of momentum and total energy, but it also recovers spherical symmetry. However, it can be shown that the GCL no longer holds (see the full derivation of Eq. (3.22)), and nor does the entropy inequality condition (3.38).

4.2 Proof of symmetry preservation

The proof of spherical symmetry is presented on an equi-angular initial grid. It needs to consider variables including the cell-center velocity, point velocity, internal energy, and density. For an equi-angular grid, the values of these variables are required to be constant along the angular direction, and the vectors are required to lie along the radial direction with time marching. Following our earlier work [28], the classical predictor–corrector time discretization method is adopted to advance time.

Theorem 4.1. *The scheme* (4.3) *can retain the one-dimensional spherical symmetry property when computed on an equi-angular initial grid. That is, if the solution has spherical symmetry at the initial time, then the symmetry will still hold with time marching.*

Proof. Without loss of generality, it is only necessary to prove that when the cell-centered Riemann solver, momentum, internal energy, and trajectory equations are known to preserve spherical symmetry at the nth step, they can retain spherical symmetry at the $(n+\frac{1}{2})$th step. For convenience of notation, variables without the superscript $(n+\frac{1}{2})$ are at the nth step.

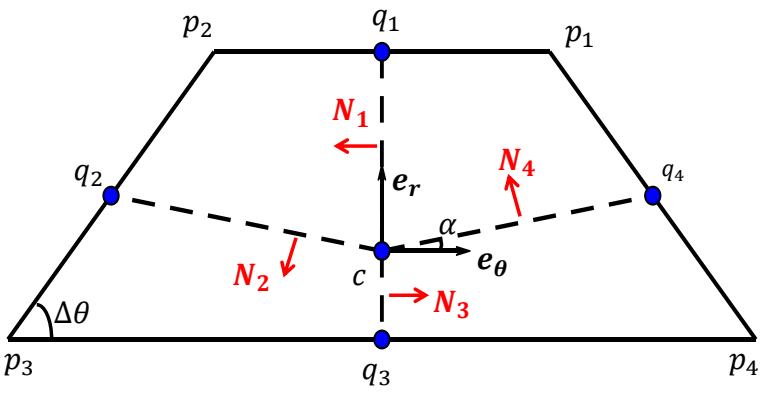

Figure 5: Quadrangle on the equi-angular grid and notation for one-dimensional spherical flow.

Here, we first show that the solution of the cell-centered Riemann solver (3.34) preserves spherical symmetry in the case of a one-dimensional flow computed on an equi-angular polar grid. As shown in Fig. 5, we consider a quadrangular cell Ω_c consisting of four points $p_i, i=1,\cdots,4$, whose velocities are $\boldsymbol{U}_{p_i}$. The midpoints of the four edges of the cell are denoted by q_i. For the edge cq_i, the edge length and radius in Eq. (3.12) are simply denoted by L_i and r_i, respectively, and the unit vectors $\boldsymbol{N}_i$ are as defined in Fig. 5. A local orthonormal basis $(\boldsymbol{e}_r,\boldsymbol{e}_\theta)$ is constructed at the cell center c, where $\boldsymbol{e}_r$ is perpendicular to the edge p_3p_4. The velocities $\boldsymbol{U}_{p_i}$ can now be represented as

$$\begin{aligned} \boldsymbol{U}_{p_1} &= U_{p_1}\begin{pmatrix}\sin\Delta\theta\\ -\cos\Delta\theta\end{pmatrix}, \quad \boldsymbol{U}_{p_2} = U_{p_1}\begin{pmatrix}\sin\Delta\theta\\ \cos\Delta\theta\end{pmatrix}, \\ \boldsymbol{U}_{p_3} &= U_{p_3}\begin{pmatrix}\sin\Delta\theta\\ \cos\Delta\theta\end{pmatrix}, \quad \boldsymbol{U}_{p_4} = U_{p_3}\begin{pmatrix}\sin\Delta\theta\\ -\cos\Delta\theta\end{pmatrix}, \end{aligned} \tag{4.4}$$

and the unit vectors $\boldsymbol{N}_i$ as

$$\begin{aligned} \boldsymbol{N}_1 &= \begin{pmatrix}0\\ -1\end{pmatrix}, \quad \boldsymbol{N}_2 = \begin{pmatrix}-\cos\alpha\\ -\sin\alpha\end{pmatrix}, \\ \boldsymbol{N}_3 &= \begin{pmatrix}0\\ 1\end{pmatrix}, \quad \boldsymbol{N}_4 = \begin{pmatrix}\cos\alpha\\ -\sin\alpha\end{pmatrix}. \end{aligned} \tag{4.5}$$

In spherical flow, it can be deduced from Eqs. (3.25)-(3.27) that the subcells $\Omega_c^{p_1}$ and $\Omega_c^{p_2}$ share the same swept mass flux Z_1 and that $\Omega_c^{p_3}$ and $\Omega_c^{p_4}$ share the same swept mass flux Z_3. The matrix M_c in Eq. (3.34) is now evaluated. After some elementary calculations, it is found that

$$\begin{aligned} M_{c,rr} &= L_2(Z_1+Z_3)(r_2+r_4)\cos^2\alpha, \\ M_{c,r\theta} &= M_{c,\theta r} = L_2(Z_1+Z_3)(r_2-r_4)\sin\alpha\cos\alpha, \\ M_{c,\theta\theta} &= 2(Z_1r_1L_1+Z_3r_3L_3)+L_2(Z_1+Z_3)(r_2+r_4)\sin^2\alpha. \end{aligned} \tag{4.6}$$

The components of the right-hand side of Eq. (3.34) are

$$\begin{aligned} RH_r &= L_2\left(Z_1U_{p_1}+Z_3U_{p_3}\right)(r_2+r_4)\cos\alpha\sin(\Delta\theta+\alpha),\\ RH_\theta &= L_2\left(Z_1U_{p_1}+Z_3U_{p_3}\right)(r_2-r_4)\sin\alpha\sin(\Delta\theta+\alpha). \end{aligned} \tag{4.7}$$

The cell-center velocity is evaluated as

$$U_{c,r}=\frac{Z_1U_{p_1}+Z_3U_{p_3}}{Z_1+Z_3}\frac{\sin(\Delta\theta+\alpha)}{\cos\alpha},\quad U_{c,\theta}=0. \tag{4.8}$$

It can be seen that *the cell-center velocity is radial and its value is constant along the angular direction, and thus the cell-center Riemann solver preserves the spherical symmetry on an equi-angular grid.*

Next, we need to prove that the evolved point velocity, internal energy, and density preserve spherical symmetry. It is known that for a dual grid (excluding that located on the z axis), the value of the mass has the following form:

$$m_p=r_pB_{i,j}, \tag{4.9}$$

where the coefficient $B_{i,j}$ is identical along the angular direction when $j\in[2,L]$. As can be seen from in Fig. 4, the momentum equation can be written as

$$m_p\boldsymbol{U}_p^{n+\frac{1}{2}}=m_p\boldsymbol{U}_p-\frac{1}{2}\Delta t\sum_{c=1}^{4}\left(\boldsymbol{F}_{cp}-\boldsymbol{S}_{cp}^*\right). \tag{4.10}$$

We now try to write out the variables appearing on the right-hand side of Eq. (4.10). The edge pressures related to $\boldsymbol{F}_{cp}$ are written as

$$\begin{aligned} \Pi_{\bar{1}}&=\Pi_{\underline{2}}=P_1-Z_{\bar{1}}(\boldsymbol{U}_1-\boldsymbol{U}_p)\cdot\boldsymbol{N}_{\bar{1}}=P_1+Z_{\bar{1}}\left(U_1\cos\alpha+U_p\sin(\Delta\theta+\alpha)\right),\\ \Pi_{\underline{1}}&=\Pi_{\bar{2}}=P_1-Z_{\underline{1}}(\boldsymbol{U}_1-\boldsymbol{U}_p)\cdot\boldsymbol{N}_{\underline{1}}=P_1+Z_{\underline{1}}U_p\cos\Delta\theta, \end{aligned} \tag{4.11}$$

where, in a local basis, $\boldsymbol{U}_1=(U_1,0)$, $\boldsymbol{U}_p=(U_p\sin\Delta\theta,-U_p\cos\Delta\theta)$, $\boldsymbol{N}_{\bar{1}}=(-\cos\alpha,\sin\alpha)$, and $\boldsymbol{N}_{\underline{1}}=(0,-1)$. It is obvious that $\Pi_{\bar{1}}$ and $\Pi_{\underline{1}}$ are identical, with the same radial point index i. According to Eq. (3.20), the sum of the source terms in subcells Ω_1^p and Ω_2^p can be written as

$$\begin{aligned} &\boldsymbol{S}_{1p}^*+\boldsymbol{S}_{2p}^*\\ =&-\left(r_{\underline{1}}L_{\underline{1}}\boldsymbol{N}_{\underline{1}}+r'_{\bar{1}}L'_{\bar{1}}\boldsymbol{N}'_{\bar{1}}+r''_{\bar{1}}L''_{\bar{1}}\boldsymbol{N}''_{\bar{1}}+r'_{\underline{2}}L'_{\underline{2}}\boldsymbol{N}'_{\underline{2}}+r''_{\underline{2}}L''_{\underline{2}}\boldsymbol{N}''_{\underline{2}}+r_{\bar{2}}L_{\bar{2}}\boldsymbol{N}_{\bar{2}}\right)\Pi_{\underline{1}}\\ &+\left(-r_{\bar{1}}L_{\bar{1}}\boldsymbol{N}_{\bar{1}}-r_{\underline{2}}L_{\underline{2}}\boldsymbol{N}_{\underline{2}}+r'_{\bar{1}}L'_{\bar{1}}\boldsymbol{N}'_{\bar{1}}+r'_{\underline{2}}L'_{\underline{2}}\boldsymbol{N}'_{\underline{2}}\right)\Pi_{\bar{1}}. \end{aligned} \tag{4.12}$$

Let $\boldsymbol{H}_a=\boldsymbol{F}_{1p}+\boldsymbol{F}_{2p}-\boldsymbol{S}_{1p}^*-\boldsymbol{S}_{2p}^*$. Then, some elementary calculations give

$$\boldsymbol{H}_a=2r_eL'_{\bar{1}}\boldsymbol{N}'_{\bar{1}}(\Pi_{\bar{1}}-\Pi_{\underline{1}})-2r_fL''_{\bar{1}}\boldsymbol{N}''_{\bar{1}}\Pi_{\underline{1}}. \tag{4.13}$$

Decomposition of the vector $\boldsymbol{H}_a$ in the local coordinate system (ξ,θ) in Fig. 4 gives

$$H_a^{\xi}=2r_eL_{\bar{1}}'(\Pi_{\bar{1}}-\Pi_{\underline{1}})+2r_fL_{\bar{1}}''\Pi_{\underline{1}},\quad H_a^{\theta}=0, \tag{4.14}$$

it is obvious that $\boldsymbol{H}_a/m_p$ is along the ξ direction, and its absolute value is

$$\left|\frac{H_a^{\xi}}{m_p}\right|=\frac{1}{B_{i,j}}\left|2L_{\bar{1}}'(\Pi_{\bar{1}}-\Pi_{\underline{1}})\frac{r_e}{r_p}+2L_{\bar{1}}''\Pi_{\underline{1}}\frac{r_f}{r_p}\right|. \tag{4.15}$$

We can deduce that in an equi-angular polar grid, this absolute value is constant along the angular direction. A similar conclusion can be drawn for the vector $\boldsymbol{H}_b=\boldsymbol{F}_{3p}+\boldsymbol{F}_{4p}-\boldsymbol{S}_{3p}^*-\boldsymbol{S}_{4p}^*$. Therefore, *the evolution of the point velocity in Eq.* (4.10) *preserves spherical symmetry on an equi-angular grid.*

Specifically, for a point p located on the z axis, the boundary condition is that the velocity component along the r direction must be zero. As shown in Fig. 4, when the ξ axis of the local coordinate system is parallel to the z axis, point p is located on the z axis. The mirror images of the subcells Ω_2^p and Ω_3^p with respect to the z axis need to be generated to satisfy the boundary condition. Let us just consider the forces acting from the subcell Ω_2^p and its mirror image Ω_1^p. The fully discretized momentum equation can be written as

$$\begin{aligned}\boldsymbol{U}_p^{n+\frac{1}{2}}&=\boldsymbol{U}_p-\frac{1}{2}\Delta t\sum_{c=1}^{2}\left(\boldsymbol{F}_{cp}-\boldsymbol{S}_{cp}^*\right)/m_p\\&=\boldsymbol{U}_p-\frac{\Delta t}{2B_{i,j}}\left[2L_{\bar{1}}'(\Pi_{\bar{1}}-\Pi_{\underline{1}})\frac{r_e}{r_p}+2L_{\bar{1}}''\Pi_{\underline{1}}\frac{r_f}{r_p}\right]\\&=\boldsymbol{U}_p-\frac{\Delta t}{2B_{i,j}}\left[2L_{\bar{1}}'(\Pi_{\bar{1}}-\Pi_{\underline{1}})\frac{d_e\sin\varphi}{d_p\sin\varphi}+2L_{\bar{1}}''\Pi_{\underline{1}}\frac{d_f\sin\varphi}{d_p\sin\varphi}\right].\end{aligned} \tag{4.16}$$

It is obvious that for points located on the z axis, $\sin\varphi=0$. We deal with this singularity by removing $\sin\varphi$ from the numerator and denominator simultaneously. In this way, the spherical symmetry of Eq. (4.10) is recovered on the z axis. Note that this operation can also be implemented in cases with nonspherical flow.

The internal energy equation at the $(n+\frac{1}{2})$th step is

$$\varepsilon_c^{n+\frac{1}{2}}=\varepsilon_c+\frac{1}{2}\Delta t\sum_{p\in\mathcal{P}(c)}\left(\boldsymbol{F}_{cp}-\boldsymbol{S}_{cp}^*\right)\cdot\boldsymbol{U}_p/m_c. \tag{4.17}$$

Here, the cell mass has the form

$$m_c=r_cB_{i+\frac{1}{2},j+\frac{1}{2}}', \tag{4.18}$$

where coefficients $B_{i+\frac{1}{2},j+\frac{1}{2}}'$ with the same $i+\frac{1}{2}$ index are identical. Let $H_c=\left(\boldsymbol{F}_{1p}-\boldsymbol{S}_{1p}^*\right)\cdot\boldsymbol{U}_p+\left(\boldsymbol{F}_{1p_3}-\boldsymbol{S}_{1p_3}^*\right)\cdot\boldsymbol{U}_{p_3}$. Similar to Eq. (4.15), the value of H_c/m_c can be proved to be constant along the angular direction. The proof is omitted here to avoid complex notation.

Therefore, *the evolution of the internal energy in Eq. (4.17) preserves spherical symmetry on an equi-angular grid.*

The coordinate and velocity of the (i,j)th point at the $(n+\frac{1}{2})$th step can be represented as

$$\boldsymbol{U}_{i,j}^{n+\frac{1}{2}}=\begin{pmatrix}U_i^{n+\frac{1}{2}}\cos\varphi\\ U_i^{n+\frac{1}{2}}\sin\varphi\end{pmatrix},\quad \boldsymbol{X}_{i,j}^{n+\frac{1}{2}}=\begin{pmatrix}X_i^{n+\frac{1}{2}}\cos\varphi\\ X_i^{n+\frac{1}{2}}\sin\varphi\end{pmatrix}, \tag{4.19}$$

and thus the volume of the $(i-\frac{1}{2},j-\frac{1}{2})$th cell is

$$V_{i-\frac{1}{2},j-\frac{1}{2}}^{n+\frac{1}{2}}=d_c^{n+\frac{1}{2}}\sin(\varphi-\Delta\varphi)\left[\left(X_i^{n+\frac{1}{2}}\right)^2-\left(X_{i-1}^{n+\frac{1}{2}}\right)^2\right]\sin\left(\frac{1}{2}\Delta\varphi\right)\cos\left(\frac{1}{2}\Delta\varphi\right), \tag{4.20}$$

where d_c is the distance from the cell center c to the origin. According to this equation, the density can be computed as

$$\rho_{i-\frac{1}{2},j-\frac{1}{2}}^{n+\frac{1}{2}}=\rho_{i-\frac{1}{2},j-\frac{1}{2}}\frac{d_c^n}{d_c^{n+\frac{1}{2}}}\frac{\left(X_i^n\right)^2-\left(X_{i-1}^n\right)^2}{\left(X_i^{n+\frac{1}{2}}\right)^2-\left(X_{i-1}^{n+\frac{1}{2}}\right)^2}. \tag{4.21}$$

It can be deduced from Eq. (4.21) that *the evolved density preserves spherical symmetry on an equi-angular grid.* The proof of the symmetry preservation property of the scheme (4.3) is thus completed. □

5 Numerical results in cylindrical coordinates

In this section, some numerical experiments are firstly conducted for the scheme (4.3) in a cylindrical coordinate system to verify its symmetry preservation property. The equi-angular polar grid, randomly distorted polar grid, and Cartesian grid are considered. Secondly, an extension of the developed scheme to non-spherical flow is presented. Comparisons are made between the schemes (3.23) and (4.3) to test their capabilities. For convenience, the two schemes are called the original and modified schemes. The ideal gas with $\gamma=5/3$ is considered for the following tests.

The spherical Sedov problem [29] consists of a flow field in which a blast wave evolves from a point explosion. In a quarter-circle region, the initial condition of this problem is set as $(\rho,\boldsymbol{U},P)=(1,0,10^{-6})$, except that the cells connected to the origin share a total internal energy of 0.2468. At final time $t=1$, the exact solution is a shock at unit radius with a peak density of 4. A reflective boundary condition is applied on the axes, with a free boundary condition being applied on the other boundaries.

The spherical Noh problem [30] is a well-known test for Lagrangian simulations with strong shock waves. In a quarter-circle region, a fluid of unit density is given an inward velocity of magnitude 1. The initial fluid pressure is set to be 10^{-6}. At $t=0$, a shock wave is reflected from the origin with a speed of $\frac{1}{3}$. The analytical post shock density is 64.

A reflective boundary condition is applied on the axes, with a free boundary condition being applied on the other boundaries.

The spherical Sod problem is a shock tube of unit radius. At $t=0$, the interface is located at $r=0.5$. The states of the left and right sides are $(\rho_L,P_L,U_L)=(1,1,0)$ and $(\rho_R,P_R,U_R)=(0.125,0.1,0)$, respectively. A wall boundary condition is applied.

The Coggeshall expansion problem considers the adiabatic compression of the ideal gas. In a quarter-circle region, the initial condition of this problem is as follows,

$$\rho=1, \quad (u_z,u_r)=(-z/4,-r), \quad e=(3z_c/8)^2,$$

where z_c is the z coordinate of the cell center. A reflective boundary condition is applied on the axes, with a free boundary condition being applied on the other boundaries.

5.1 One dimensional spherical flows

5.1.1 Equi-angular polar grid

For the Sedov problem, the results of the original and modified schemes for a 20×20 grid are presented in Fig. 6. It is obvious that with the original scheme, grid points near the origin do not preserve spherical symmetry. However, with the modified scheme, the simulated grid preserves good symmetry. For a fine 200×40 grid, the symmetry error of the pressure is computed as

$$\delta=\left[\max_{i\in[1,K+1]}\left(\max_{j\in[1,L+1]}\frac{P_{i-\frac{1}{2},j-\frac{1}{2}}L}{\sum_{j=1}^{L+1}P_{i-\frac{1}{2},j-\frac{1}{2}}}\right)-1\right]. \tag{5.1}$$

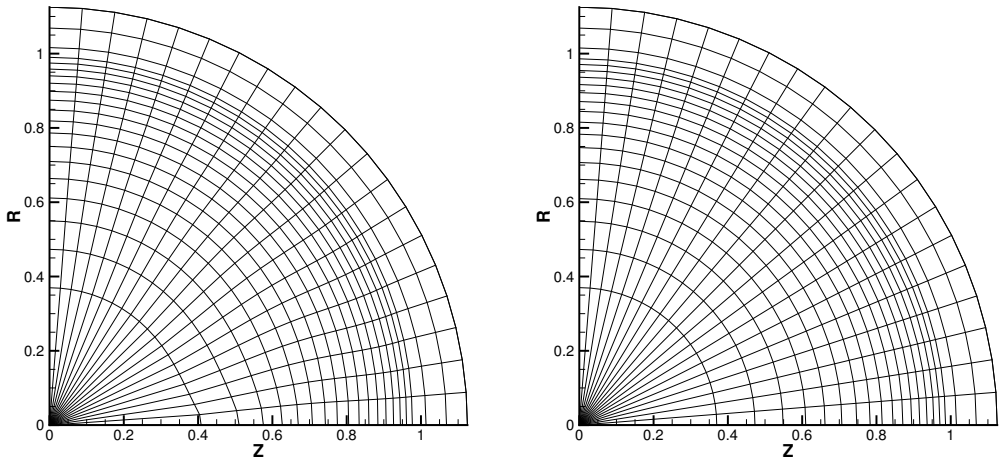

(a) (b)

Figure 6: Simulated grids for the Sedov problem at $t=1$ for an initial 20×20 polar grid: (a) original scheme; (b) modified scheme.

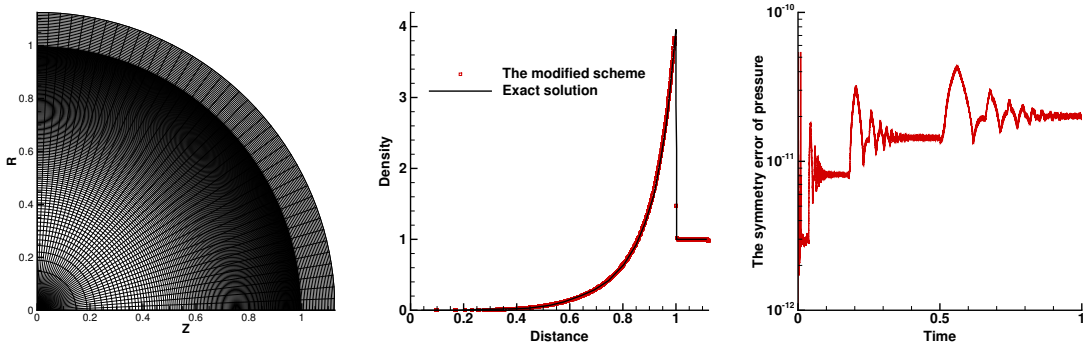

(a) (b) (c)

Figure 7: Results of Sedov problem at $t=1$ for an initial 200×40 polar grid: (a) final grid; (b) density–radius profile; (c) pressure error.

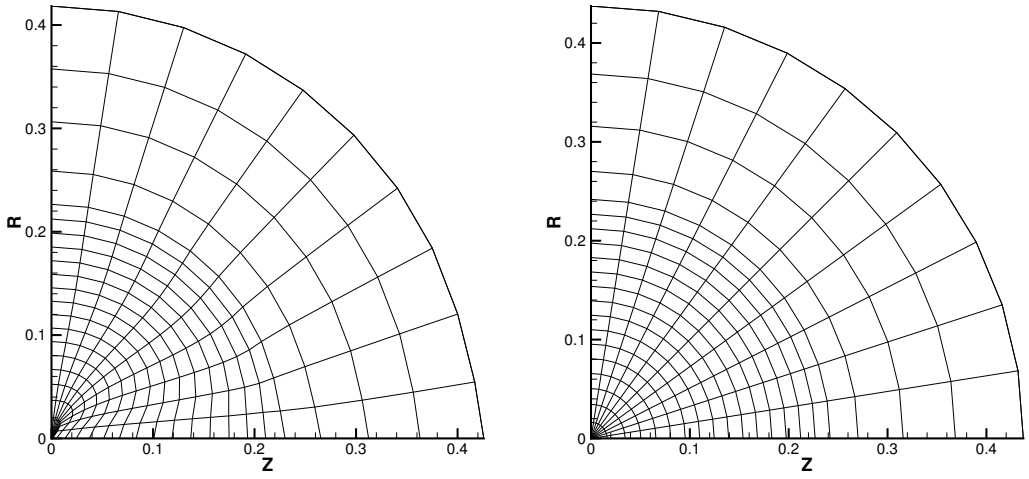

(a) (b)

Figure 8: Simulated grids for the Noh problem at $t=0.6$ for an initial 20×10 polar grid: (a) original scheme; (b) modified scheme.

Fig. 7 presents the results for the fine grid. At $t=1$, the simulated grid still preserves good symmetry, and the numerical results is convergent to the analytical solution. In addition, the symmetry error on the pressure is less than 10^{-10}, which shows the symmetry preservation property of the modified scheme.

For the Noh problem, the results of the original and modified schemes for a 20×10 grid are presented in Fig. 8. With the original scheme, points run inward faster, especially near the z axis, while with the modified scheme, points run inward uniformly along

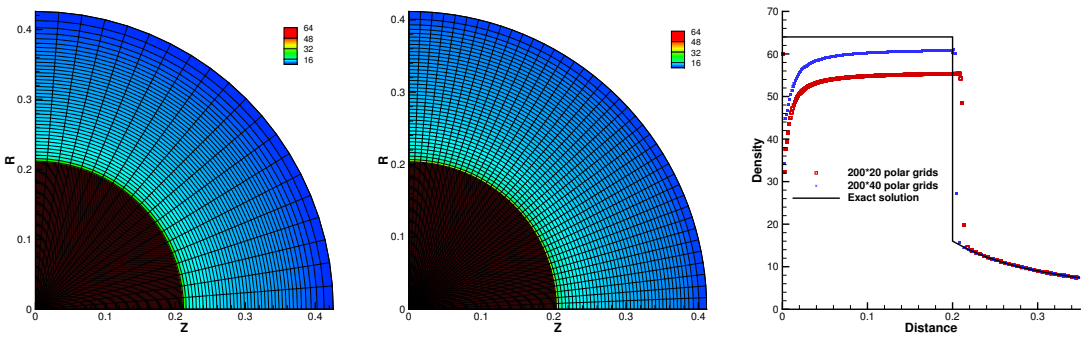

(a) (b) (c)

Figure 9: Results for Noh problem at $t=0.6$ for initial 200×20 and 200×40 polar grids. (a) 200×20 density field; (b) 200×40 density field; (c) density–radius profile.

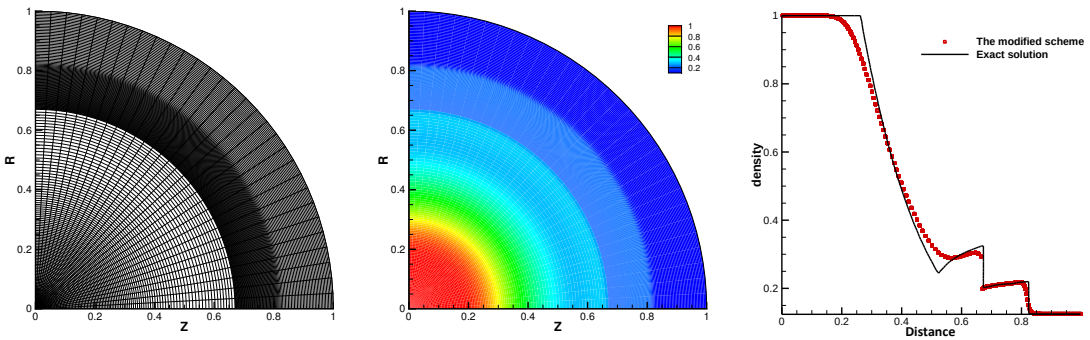

(a) (b) (c)

Figure 10: Results for Sod problem at $t=0.2$ for an initial 200×30 polar grid: (a) final grid; (b) final density field; (c) density–radius profile.

the angular direction. The spherical symmetry is further examined for the 200×20 and 200×40 grids, and the results are presented in Fig. 9. It is observed that symmetry is perfectly preserved. As the angular division increases, better convergence of the numerical solutions toward the analytical solution is achieved.

The Sod problem is simulated on a 200×30 polar grid, and the results of the modified scheme are presented in Fig. 10. From the configurations of the final grid and density field, it can be seen that there is good agreement with the spherical shape. By using a one-dimensional spherical second-order Eulerian code with 10000 grid points as the reference solution, we found the simulated density–radius profile agrees well with the reference.

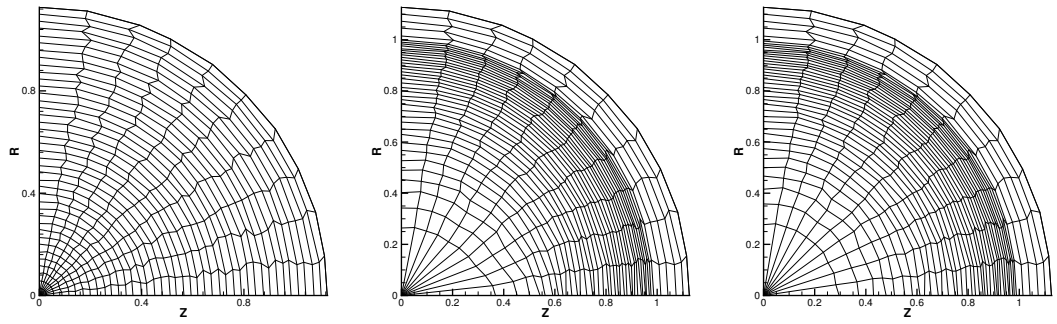

(a) (b) (c)

Figure 11: Results for the Sedov problem at $t=1$ for an initial 40×10 random polar grid: (a) initial grid; (b) final grid for original scheme; (b) final grid for modified scheme.

5.1.2 Random distorted polar grid

We perform a simulation for the Sedov problem on a randomly distorted 40×10 polar grid. Fig. 11(a) shows the initial distorted grid, and Fig. 11(b) and 11(c) show the final grids for the original and modified schemes, respectively. It can be seen that better spherical preservation of the grid is achieved by the modified scheme, especially around the z axis.

It is found that the Noh problem is very sensitive to grid perturbation. In this case, a small perturbation is implemented to generate the initial grid for the Noh problem, which is shown in Fig. 12(a). The final grids of the original and modified schemes at $t=0.6$ are shown in Fig. 12(b) and 12(c). It can be seen that better agreement with the spherical shape is displayed by the grid of the modified scheme. In addition, Fig. 12(d) shows that the convergence of the density–radius profile is better with the modified scheme.

5.1.3 Cartesian grid

The Noh problem is a difficult test for a Cartesian grid, since grid distortions might occur because the flow is not aligned with the grid. In our case, it is run on a 40×40 Cartesian grid. Fig. 13 presents the density fields of the original and modified schemes at $t=0.6$. As can be seen, severe grid distortions are observed around the z axis, indicating a poor performance of the original scheme. On the other hand, the modified scheme maintains good mesh quality, and the shock position is observed to agree well with the analytical solution.

5.2 Non-spherical flow

In non-spherical flows, the treatment of source term is also implemented using Eq. (4.2), where $\Pi_{\underline{1}}$ and $\Pi_{\overline{1}}$ are pressures of radial and tangential edges. Practically, either edge of $1d$ and $1a$ has a smaller angle with the point velocity $\boldsymbol{U}_p$ is considered as the radial edge.

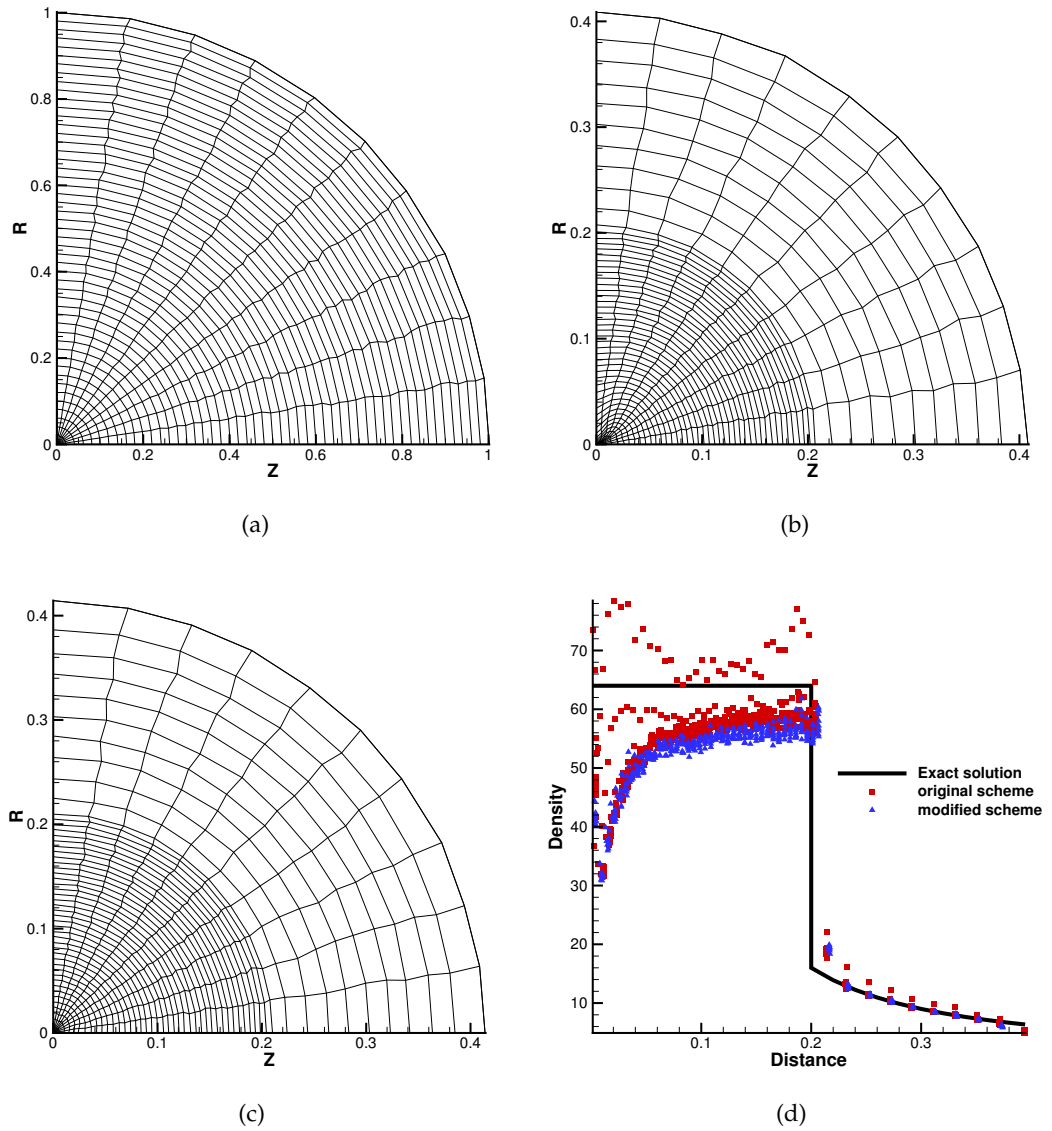

Figure 12: Results for the Noh problem at $t=0.6$ for an initial 50×10 random polar grid: (a) initial grid; (b) final grid of original scheme; (c) final grid of modified scheme; (d) density plots of the two schemes.

The other edge is considered as the tangential edge. Note that the range of included angle is $[0,\pi/2]$. The results of the original and modified schemes for a 100×10 grid are presented in Fig. 14. At $t=0.8$, the analytical density is 37.4. Small difference of the final grid is observed between the original and modified scheme. However, the numerical results of the modified scheme agree a little bit better with the analytical solution, which confirm the capacity of the new scheme in non-spherical flows.

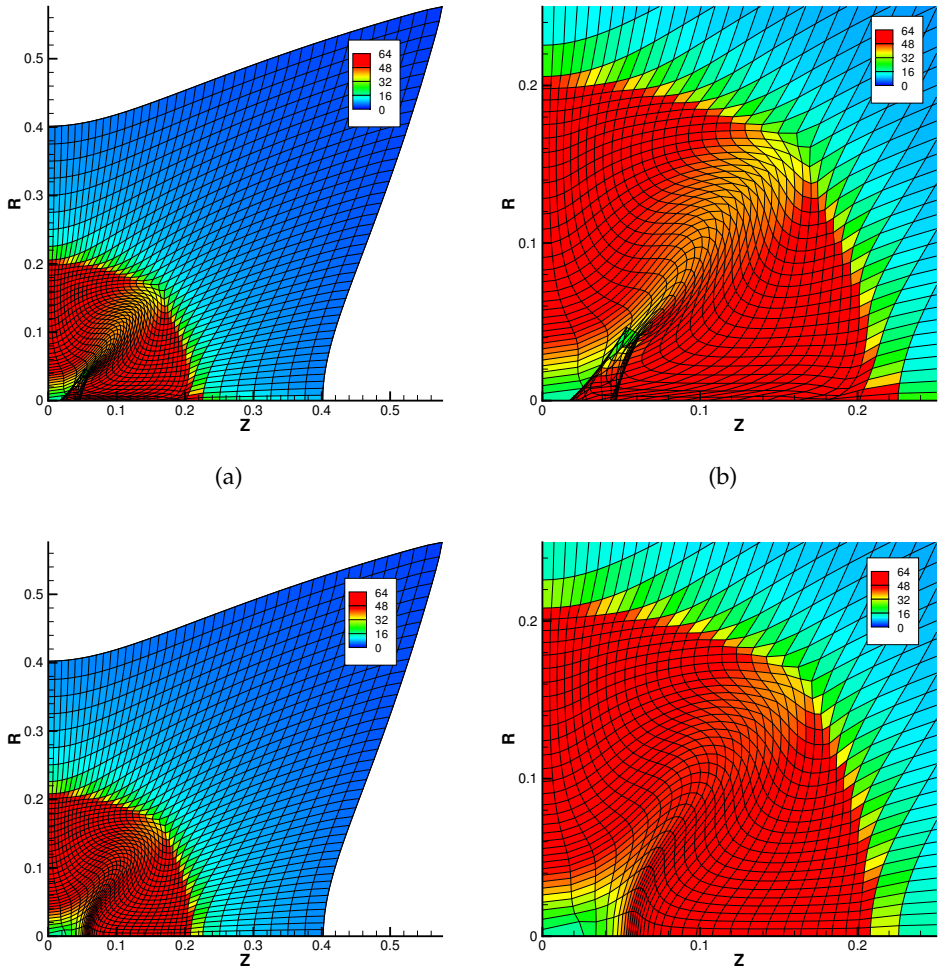

Figure 13: Results for the Noh problem at $t=0.6$ for an initial 40×40 Cartesian grid: (a) density map of original scheme; (b) zoom of (a); (c) density map of modified scheme; (d) zoom of (c).

6 Conclusions

We first constructed a control-volume scheme satisfying the GCL, entropy inequality, and momentum and total energy conservation. The spherical symmetry property of this scheme was recovered by a proper treatment of the source term, while still ensuring momentum and total energy conservation. The modified scheme was shown to preserve one-dimensional spherical symmetry on an equi-angular polar grid. Numerical results of the modified scheme in cylindrical coordinates showed that it has good performance in symmetry preservation, as well as good potential application in non-spherical flows.

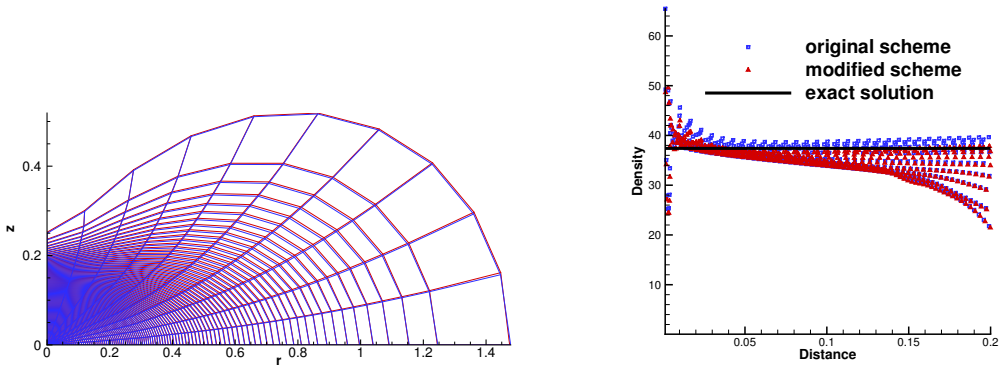

Figure 14: Results for the Coggeshall problem at $t=0.8$. Left: final grid. Blue for the original scheme, and red for the modified scheme; Right: density plots of the two schemes.

In the future, we will test the capabilities of the current scheme by extending it to more non-spherical flows. In addition, the artificial viscosity used in the current scheme is not limited to a Godunov-type artificial viscosity, and, for other viscosities, once the source term has been modified to exclude any angular influence on updating the momentum equation, similar effects of symmetry preservation should be achievable.

Acknowledgments

This project is supported by the National Natural Science Foundation of China (12201055). The authors thank the reviewer's valuable suggestions during the revision of this paper.

References

[1] E. Caramana, D. Burton, M. Shashkov, P. Whalen, The construction of compatible hydrodynamics algorithms utilizing conservation of total energy, Journal of Computational Physics 146 (1) (1998) 227–262. doi:10.1006/jcph.1998.6029.

[2] E. Caramana, C. Rousculp, D. Burton, A compatible, energy and symmetry preserving Lagrangian hydrodynamics algorithm in three-dimensional Cartesian geometry, Journal of Computational Physics 157 (1) (2000) 89–119.

[3] R. Loubère, M. Shashkov, B. Wendroff, Volume consistency in a staggered grid Lagrangian hydrodynamics scheme, Journal of Computational Physics 227 (8) (2008) 3731–3737.

[4] P. H. Maire, A high-order cell-centered Lagrangian scheme for compressible fluid flows in two-dimensional cylindrical geometry, Journal of Computational Physics 228 (18) (2009) 6882–6915.

[5] N. R. Morgan, K. N. Lipnikov, D. E. Burton, M. A. Kenamond, A Lagrangian staggered grid Godunov-like approach for hydrodynamics, Journal of Computational Physics 259 (2014) 568–597.

[6] D. E. Burton, N. R. Morgan, T. C. Carney, M. A. Kenamond, Reduction of dissipation in Lagrange cell-centered hydrodynamics (CCH) through corner gradient reconstruction (CGR), Journal of Computational Physics 299 (2015) 229–280.
[7] M. Dumbser, W. Boscheri, High-order unstructured Lagrangian one-step WENO finite volume schemes for non-conservative hyperbolic systems: Applications to compressible multiphase flows, Computers & Fluids 86 (2013) 405–432.
[8] M. Kenamond, M. Bement, M. Shashkov, Compatible, total energy conserving and symmetry preserving arbitrary Lagrangian–Eulerian hydrodynamics in 2D rz–Cylindrical coordinates, Journal of Computational Physics 268 (2014) 154–185.
[9] A. J. Barlow, P.-H. Maire, W. J. Rider, R. N. Rieben, M. J. Shashkov, Arbitrary Lagrangian–Eulerian methods for modeling high-speed compressible multimaterial flows, Journal of Computational Physics 322 (2016) 603–665.
[10] D. E. Burton, N. R. Morgan, M. R. J. Charest, M. A. Kenamond, J. Fung, Development of a compatible, energy conserving, bounds preserving remap of hydrodynamic fields in a generalized ALE scheme, Tech. rep., Los Alamos National Lab.(LANL), Los Alamos, NM (United States) (2017).
[11] V. Chiravalle, N. Morgan, A 3D finite element ALE method using an approximate Riemann solution, International Journal for Numerical Methods in Fluids 83 (8) (2017) 642–663.
[12] F. Wu, R. Ramis, Z. Li, A conservative MHD scheme on unstructured lagrangian grids for Z-pinch hydrodynamic simulations, Journal of Computational Physics 357 (2018) 206–229.
[13] S. Guo, M. Zhang, H. Zhou, J. Xiong, S. Zhang, A symmetry preserving scheme for three-dimensional Lagrangian radiation hydrodynamic simulations of ICF capsule implosion, Computers & Fluids 195 (2019) 104317.
[14] A. Marboeuf, A. Claisse, P. Le Tallec, Conservative and entropy controlled remap for multimaterial ALE simulations with space-staggered schemes, Journal of Computational Physics 390 (2019) 66–92.
[15] V. Gyrya, E. Lieberman, M. A. Kenamond, M. J. Shashkov, Optimization of artificial viscosity in production codes based on Gaussian Regression surrogate models, Tech. rep., Los Alamos National Lab.(LANL), Los Alamos, NM (United States) (2022).
[16] J. Cheng, C.-W. Shu, A cell-centered Lagrangian scheme with the preservation of symmetry and conservation properties for compressible fluid flows in two-dimensional cylindrical geometry, Journal of Computational Physics 229 (19) (2010) 7191–7206.
[17] J. Cheng, C.-W. Shu, Improvement on spherical symmetry in two-dimensional cylindrical coordinates for a class of control volume Lagrangian schemes, Communications in Computational Physics 11 (4) (2012) 1144–1168.
[18] J. Cheng, C.-W. Shu, Second order symmetry-preserving conservative Lagrangian scheme for compressible Euler equations in two-dimensional cylindrical coordinates, Journal of Computational Physics 272 (2014) 245–265.
[19] P.-H. Maire, I. Bertron, R. Chauvin, B. Rebourcet, Thermodynamic consistency of cell-centered Lagrangian schemes, Computers & Fluids 203 (2020) 104527.
[20] A. Barlow, D. Burton, M. Shashkov, Compatible, energy and symmetry preserving 2D Lagrangian hydrodynamics in rz-cylindrical coordinates, Procedia Computer Science 1 (1) (2010) 1893–1901.
[21] E. Caramana, P. Whalen, Numerical preservation of symmetry properties of continuum problems, Journal of Computational Physics 141 (2) (1998) 174–198.
[22] P. Váchal, B. Wendroff, On preservation of symmetry in r–z staggered Lagrangian schemes, Journal of Computational Physics 307 (2016) 496–507.

[23] L. Margolin, M. Shashkov, Using a curvilinear grid to construct symmetry-preserving discretizations for Lagrangian gas dynamics, Journal of Computational Physics 149 (2) (1999) 389–417.
[24] V. A. Dobrev, T. E. Ellis, T. V. Kolev, R. N. Rieben, High-order curvilinear finite elements for axisymmetric Lagrangian hydrodynamics, Computers & Fluids 83 (2013) 58–69.
[25] P.-H. Maire, N. Therme, Weak consistency of a staggered finite volume scheme for Lagrangian hydrodynamics, SIAM Journal on Numerical Analysis 58 (3) (2020) 1592–1612.
[26] P. P. Whalen, Algebraic limitations on two-dimensional hydrodynamics simulations, Journal of Computational Physics 124 (1) (1996) 46–54.
[27] P.-H. Maire, R. Loubère, P. Váchal, Staggered Lagrangian discretization based on cell-centered Riemann solver and associated hydrodynamics scheme, Communications in Computational Physics 10 (4) (2011) 940–978. doi:10.4208/cicp.170310.251110a.
[28] C. Xu, Q. Zeng, J. Cheng, A Godunov-type tensor artificial viscosity for staggered Lagrangian hydrodynamics, Journal of Computational Physics 426 (2021) 109666.
[29] L. I. Sedov, M. Friedman, M. Holt, J. Cole, Similarity and dimensional methods in mechanics.
[30] W. F. Noh, Errors for calculations of strong shocks using an artificial viscosity and an artificial heat flux, Journal of Computational Physics 72 (1) (1987) 78–120.